Role of local flow conditions in river biofilm colonization and early growth

Falilou Coundoul, Thomas Bonometti, Myriam Graba, Sabine Sauvage, J.M. Sánchez-Pérez, Frédéric Moulin

▶ **To cite this version:**

Falilou Coundoul, Thomas Bonometti, Myriam Graba, Sabine Sauvage, J.M. Sánchez-Pérez, et al.. Role of local flow conditions in river biofilm colonization and early growth. River Research and Applications, 2014, 31 (3), pp.350-367. 10.1002/rra.2746 . hal-02930248

HAL Id: hal-02930248
https://hal.science/hal-02930248v1

Submitted on 4 Sep 2020

HAL is a multi-disciplinary open access archive for the deposit and dissemination of scientific research documents, whether they are published or not. The documents may come from teaching and research institutions in France or abroad, or from public or private research centers.

L'archive ouverte pluridisciplinaire **HAL**, est destinée au dépôt et à la diffusion de documents scientifiques de niveau recherche, publiés ou non, émanant des établissements d'enseignement et de recherche français ou étrangers, des laboratoires publics ou privés.

Open Archive Toulouse Archive Ouverte (OATAO)

OATAO is an open access repository that collects the work of Toulouse researchers and makes it freely available over the web where possible.

This is an author-deposited version published in: http://oatao.univ-toulouse.fr/
Eprints ID: 11798

Identification number: DOI: 10.1002/rra.2746
fficial URL: http://dx.doi.org/10.1002/rra.2746

To cite this version:
Coundoul, Falilou and Bonometti, Thomas and Graba, Myriam and Sauvage, Sabine and Sanchez-Pérez, José-Miguel and Moulin, Frédéric *Role of local flow conditions in river biofilm colonization and early growth.* (2014) River Research and Applications . ISSN 1535-1459

Any correspondence concerning this service should be sent to the repository administrator:
staff-oatao@inp-toulouse.fr

ROLE OF LOCAL FLOW CONDITIONS IN RIVER BIOFILM COLONIZATION AND EARLY GROWTH

F. COUNDOUL[a], T. BONOMETTI[a], M. GRABA[b,c], S. SAUVAGE[b,c], J.-M. SANCHEZ PÉREZ[b] AND F. Y. MOULIN[a]*

[a] *Institut de Mécanique des Fluides de Toulouse, Université de Toulouse, INPT, UPS; CNRS, Allée du Professeur C. Soula 31400 Toulouse, France*
[b] *Universitéde Toulouse, INPT, UPS; EcoLab, 31326 Castanet-Tolosan, France*
[c] *CNRS, EcoLab, 31062 Toulouse, France*

ABSTRACT

Direct numerical simulations of a turbulent boundary layer flow over a bed of hemispheres of height h are performed using an immersed boundary method for comparison with river biofilm growth experiments performed in a hydraulic flume. Flow statistics above the substrates are shown to be in agreement with measurements performed by laser Doppler velocimetry and particle image velocimetry in the experiments. Numerical simulations give access to flow components inside the roughness sublayer, and biofilm colonization patterns found in the experiments are shown to be associated with low shear stress regions on the hemisphere surface. Two bed configurations, namely staggered and aligned configurations, lead to different colonization patterns because of differences in the local flow topology. Dependence with the Reynolds number of the biofilm distribution and accrual 7 days after inoculum is shown to be associated to local flow topology change and shear stress intensity. In particular, the shear stress τ on the surface of the hemispheres is found to scale as $\mu(u^*/h)Re_t^{0.26}$, where $Re_t = u^* h/\nu$, with u^* as the log law friction velocity and ν as the fluid kinematic viscosity. This scaling is due to the development of boundary layers along the hemisphere surface. Associated with a critical shear stress for colonization and early growth, it explains the increasing delay in biomass accrual for increasing flow velocities in the experiments.

KEY WORDS: turbulent boundary layer; river biofilm; roughness sublayer; canopy flow

INTRODUCTION

The epilithic biofilm, an aggregate set of phototrophic organisms growing on the bed of rivers, plays an essential role in the functioning of river ecosystems: storage of nutrients, carbon and nitrogen cycle and nutrients resource for higher trophic. To improve the modelling of hydro-ecosystems such as the Garonne River (Boulêtreau *et al*., 2008), it is necessary to introduce a functional compartment for the biofilm and to adequately describe its interaction with the flow. This is also true for improving the management of artificial waterways such as irrigation channels where the growth of biofilm and its detachment can caused significant problems (Fovet *et al*., 2010).

Hydrodynamics has been early recognized as one of the most important environmental factors controlling stream biofilm dynamics and structure and is considered the major physical forcing on the biofilm (Reiter, 1986; Power and Stewart, 1987; Biggs *et al*., 2005, 2008). Firstly, access to nutrients for the biofilm is controlled by the thickness of the diffusive boundary layer that develops in its vicinity, a layer that is related to the flow water velocity field (see, e.g. Riber and Wetzel, 1987). Secondly, as water velocity increases, drag force and skin friction exerted on the community control its attachment ability (Biggs and Hickey, 1994; Biggs and Thomsen, 1995). The effect of water velocity has been analysed in a large number of studies, both in natural streams (Biggs and Hickey, 1994; Uehlinger *et al*., 1996; Boulêtreau *et al*., 2006, 2008) and in flumes (Ghosh and Gaur, 1998; Hondzo and Wang, 2002). Only local flow conditions are ultimately relevant for describing the forcing at biofilm scale, and they are generally not easily inferred from mean bulk velocities. Yet, in most of the field and laboratory studies on flow–biofilm interactions, mainly for practical reasons and for easy integration in large-scale flow modelling (using shallow water equations), the flow characterization is global and obtained either by measuring a 'stream' velocity defined generally as an averaged value measured at $z = 0.4D$ from the bottom, where D is the water depth (Biggs and Hickey, 1994; Takao *et al*., 2008), or by calculating a bulk velocity from the flow rate Q divided by the river cross-sectional area S (Cazelles *et al*., 1991; Kim *et al*., 1992; Biggs *et al*., 1997; Claret and Fontvieille, 1997; Ghosh and Gaur, 1998; Battin and Sengschmitt, 1999; Robinson *et al*., 2004; Luce *et al*., 2010) or finally by using the flow rate Q directly (Matthaei *et al*., 2003; Boulêtreau *et al*., 2006).

*Correspondence to: F. Y. Moulin, Institut de Mcanique des Fluides de Toulouse, Universit de Toulouse, INPT, UPS; CNRS, Alle du Professeur C. Soula, 31400 Toulouse, France.
E-mail: Frederic.Moulin@imft.fr

DOI: 10.1002/rra.2746

Very few field studies (see the review by Biggs *et al*., 1998) attempted to characterize the flow close to the bed (velocity measurements within 2 mm of the substrata in the study of Biggs *et al*., 1998, using hot-film anemometry). These studies clearly showed that the near-bed velocities were far better correlated to the biofilm dynamics than the global flow velocities. As Biggs *et al*. (1998) pointed out in their conclusion, 'This suggests that it may not be possible to define clear velocity–biomass relationships in streams with high relative roughness using standard flow-measuring technology. This may also explain some of the wide variation in relationships previously reported in the literature (Stevenson *et al*., 1996). "Under such conditions of high bed roughness, a biomass–velocity function based on the mean near-bed velocity is a more useful discriminator of forces near the bed than shear velocity from the logarithmic formula". This statement, along with qualitative observations in field studies of the strong link between local flow conditions and biofilm growth, supported the use of mesocosms for a better quantification of the local flow conditions and the link between biofilm dynamics and near-bed flow characteristics. For river biofilms growing on artificial or small-scale sediment beds, a vertical profile of mean velocity and/or turbulent statistics is sufficient to describe correctly the near-bed flow conditions, that is, down to the top of the roughness sublayer where the flow becomes strongly three dimensional (Florens *et al*., 2013). Such measurements along vertical profiles were then successfully used to investigate the relationship between hydrodynamics and biofilm growth: Biggs and Thomsen (1995) studied the resistance of different biofilm communities to increasing shear stress, Nikora *et al*. (2002) quantified the impact of growing biofilm on concrete on the turbulent boundary layer structure and hydraulic roughness, and Hondzo and Wang (2002) inferred a relationship between biofilm growth dynamics and local flow conditions. In these studies, the most striking result was the ability of the biofilm to modify the turbulent boundary layer parameters, especially the roughness length z_0 (or, equivalently, the hydraulic roughness k_s, as $k_s \approx 32 z_0$). However, because of the intrinsic three dimensionality of the near-bed flow associated with the presence of a roughness sublayer developing above large rough substrates and biofilm itself, a methodological improvement was necessary to describe correctly the flow characteristics there. To this end, the pioneering work of Raupach *et al*. (1991) for atmospheric flows over vegetal canopies was adapted by Nikora *et al*. (2002) to river flows by promoting the now called double-averaged Navier–Stokes equations (DANS), based on both temporal and spatial horizontal averaging, a theoretical framework summarized in Nikora *et al*. (2007a, 2007b).

The local interaction between the biofilm and the water flow was not previously taken into account explicitly in predictive models for biofilm biomass accrual. Most of these models (Horner *et al*. 1983; Uehlinger *et al*., 1996; Saravia *et al*., 1998; Asaeda and Hong Son, 2001) are indeed conceptualized models of the main processes involved, which can be summarized by an equation reading $dB/dt = C + G - D$ where B is the biofilm biomass, C the colonization function, G the growth function and D the detachment function. In most studies, the dependence of the right term functions with flow conditions is expressed using bulk quantities such as the bulk stream velocity or flow rate, mostly in the detachment function D. Recently, it was shown by Labiod *et al*. (2007) and Graba *et al*. (2010) that taking into account the local characteristics of the hydrodynamic through the turbulent boundary layer parameters (the friction velocity u^*, hydraulic roughness k_s and the displacement height d) led to better predictions than when depth averaged hydrodynamic quantities (flow rate Q and average velocity u_m) were used. The importance of local flow conditions on biofilm growth and structure was also put in evidence both in field study (Boulêtreau *et al*., 2011; Graba *et al*., 2014) and in mesocosms (Moulin *et al*., 2008; Graba *et al*., 2013). In the experimental studies in mesocosms of Boulêtreau *et al*. (2010), Graba *et al*. (2010), Moulin *et al*. (2008) and Graba *et al*. (2013), colonization patterns were also shown to be strongly dependent on local flow conditions at the bottom roughness scale, far inside the roughness boundary layer, with preferential locations put in evidence during the first week of biofilm colonization and growth for two different substrate arrangements. Because the accrual rate in the early stage of biofilm growth may be used as a functional indicator for river systems, it becomes crucial to study the dependence with local flow conditions at the substrate scale in order to distinguish the effects of river use (contaminants and anthropic inputs) from the effects of substrate and near-substrate flow topology. However, access to the velocity field near the colonized substrates is extremely difficult, even with particle image velocimetry (PIV) or LDV measurements in mesocosms (like in Moulin *et al*., 2008; Graba *et al*., 2013; or Nikora *et al*., 2002). Such measurements only give access to the upper part of the three-dimensional roughness sublayer, because of metrological or security limitations.

Fortunately, biofilm in the colonization and early growth stage remains thin enough for its impact on the flow dynamics around the substrates to be negligible, and numerical solvers can be used to perform direct numerical simulations of turbulent boundary layers of flows in mesocosms even at large Reynolds number. Such simulations provide flow components in the region above the hemispheres, where experimental measurements are available for comparison, and also deep inside the canopy region, where three-dimensional flow topology drives the colonization and early growth of biofilm. A suitable numerical approach is to use an immersed boundary method (IBM) to describe the hemispheres and fine meshes to capture

the finest scales of the turbulence. An IBM was recently implemented in the JADIM numerical solver developed at IMFT, Toulouse, France (see Calmet and Magnaudet, 2003, and Bigot *et al*., 2012), and this code was then chosen to perform the numerical simulation presented in the present study.

This study was conducted with two main objectives: (i) perform fully resolved 3D numerical simulations at high Reynolds number of turbulent boundary layer flows over a bed of hemispheres with the same flow parameters as in the studies of Boulêtreau *et al*. (2010), Graba *et al*. (2010), Moulin *et al*. (2008) and Graba *et al*. (2013) and (ii) determine the relation between the local flow conditions and the specific colonization patterns observed experimentally in these two studies in order to improve the modelling of biofilm colonization and early growth.

MATERIALS AND METHODS

Experiments

Experimental setup. To study, under controlled hydrodynamics conditions, the dynamics of epilithic river biofilm, two experiments were performed in an indoor laboratory flume at IMFT. Water flow can be partially recirculated in the Garonne River in order to avoid nutrient limitation while controlling the hydrodynamical conditions. The experimental flume was built with Plexiglas sides (10 mm thick) and a PVC base (20 mm thick). The flume is 11 m long, 0.5 m wide and 0.2 m deep, with a 10^{-3} slope. A first pump continuously supplies water from the river to the outlet reservoir (3300 L), and a second submerged pump supplies water to the inlet reservoir (1500 L) with a fixed flow rate Q. The water flows between the two reservoirs through the experimental flume by gravity. The suspended matter present in the Garonne River water was eliminated by two centrifugal separators and was then filtered. Illumination was supplied by three sets of 1.6 m-long horticultural fluorescent tubes, in a 12-h day : 12-h night photoperiod. For all experiments, the biofilm was saturated in light and nutrients in order to limit the influence of these parameters on its growth. The bottom of the flume was completely covered by artificial hemispherical cobbles of sand-blasted polyurethane resin. The artificial cobbles were $\Phi = 37$ mm in diameter and $h = 20$ mm in height.

The distribution of hemispheres at the bottom of the tank is different in the two experiments, as shown in Figure 1, and will be named aligned and staggered for the first and second experiment, respectively, according to the classification of Coceal *et al*. (2006). The staggered configuration is obtained by a 90° rotation of the aligned configuration. In the first experiment (see details in Boulêtreau *et al*., 2010),

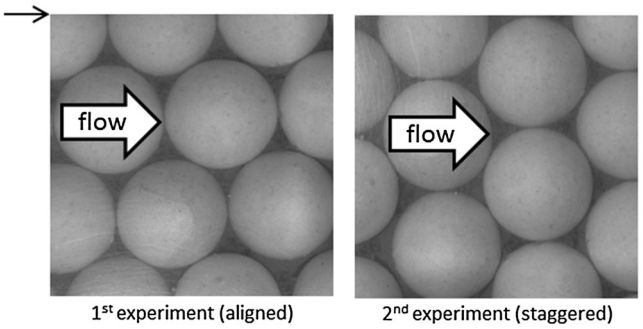

Figure 1. Hemisphere pattern configurations: (a) aligned in the first experiment (see Boulêtreau *et al*., 2010) and (b) staggered in the second experiment (see Moulin *et al*., 2008). The flow direction is from left to right

a mean bulk velocity of 0.22 m/s and a water depth $D = 13$ cm were prescribed using a flow rate $Q = 14.5$ L/s. Flow measurements yield a friction velocity of 2.8 cm/s on nude hemispheres. In the second experiment (see details in Moulin *et al*., 2008, and Graba *et al*., 2013), the flume was adapted to have three different flow conditions by modifying its width and depth. With a flow rate $Q = 6$ L/s, three mean bulk velocities (0.10, 0.275 and 0.405 m/s in the corresponding LV or low-velocity, IV or intermediate-velocity and HV or high-velocity sections) were generated, with a water depth D equal to 12.5, 8.5 and 5.5 cm, respectively. The friction velocity values inferred from flow measurements were respectively equal to 0.85, 2.61 and 4.49 cm/s. The flow regime in the IV section was chosen in order to generate a turbulent boundary layer with the same friction velocity u^* as in the first experiment.

The experiments are code named in the form of *LV*, *IV* and *HV* as a reference to values of the friction velocity around 1, 2.5 and 4.5 cm/s, respectively, and *A* or *S* for the aligned or staggered configurations, followed by a number indicating the aspect ratio D/h, where D is the water depth and h the hemisphere height. With this convention, the flow in the first experiment will be referred to as $IV_{A6.5}$, and the three flow regimes in the second experiment as $LV_{S6.5}$, $IV_{S4.25}$ and $HV_{S2.75}$. The same code will be used for the numerical simulations described later.

Flow measurements. In the first experiment (see Graba *et al*., 2010), velocity components were measured at the centerline of the flume by laser Doppler anemometry (LDA), in a section equipped with glass windows located at 8 m from the flume entrance. Measurement points were situated at heights varying from 20 to 120 mm from the bottom with a space step 2 mm between $z = 20$ and 50 mm and a space step 10 mm up to $z = 120$ mm along three vertical profiles chosen to estimate double-averaged quantities as defined by Nikora *et al*. (2007a). For each measurement point, a 4-min acquisition of around 10^4

instantaneous longitudinal and vertical velocity components u and w was performed, in order to achieve sufficient statistical convergence of mean quantities (time-averaged velocity components U and W) and turbulent quantities [the root-mean-square (RMS) values of the turbulent longitudinal and vertical fluctuations u_{rms} and w_{rms}, and the mean turbulent shear stress $\overline{u'w'}$]. Following the methodology of Nikora *et al*. (2007a), double-averaged quantities, that is, quantities averaged in the two horizontal directions and noted with brackets $< \ldots >$, were then estimated using space averaging with weight factors of 1, 2 and 1 for the measurements in the three vertical profiles, in agreement with the geometric arrangement of the hemispheres. In the second experiment (see Moulin *et al*., 2008, and Graba *et al*., 2013), velocity components were measured near the centerline of the flume by PIV in two vertical planes in the middle of the tank (one longitudinally aligned plane just at the top of the hemispheres, and another one 1 cm apart) in the three different sections. Each vertical plane yields 120 vertical profiles along around 8 cm, that is, two hemisphere diameters in the streamwise direction. Sequences of around 1000 decorrelated image pairs were treated and time averaged to extract reliable estimations of the flow statistics (U, W, u_{rms}, w_{rms} and $\overline{u'w'}$). Double-averaged quantities were estimated by spatial averaging along the streamwise direction and between the two vertical planes.

Biofilm algal composition, biomass and distribution. In the first experiment, the *inoculum* was prepared by scraping biofilm from pebbles collected in southwest France streams [Arige (09) and Gave de Pau (05)] and rivers [Garonne (7) and Tarn (8)], in order to obtain very diverse epilithic biofilm communities. Fifteen pebbles of average size of 10 cm^2 were randomly selected for the *inoculum* preparation. The biofilm suspension obtained by scraping was crushed and homogenized (tissue homogenizer) in order to get as close as possible to grazer-free initial conditions (no macrofauna). The algal community in the biofilm that grew on the pebbles was almost completely dominated by diatoms. The two dominant taxa along the whole experiment were *Fragilaria capucina* and *Encyonema minutum*, which represented, respectively, 64% and 19% of the total community during the initial growth stage (before 30 days after *inoculum*). More details are given in Graba *et al*. (2010) on the algal composition of the biofilm.

In the second experiment, the same protocol was adopted for the flume seeding, except that only the pebbles from the Garonne River were used. In this experiment, the analysis of algal communities was performed only at the end of the experiment, 37 days after *inoculum*. The dominant species was *Melosira moniliformis* (O.F.Muller) Agardh in eight of the nine samples (taken along the three contrasted flow conditions) between 14.32% and 26.95%, followed by *F. capucina var. mesolepta* (Rabh) Rabenhorst that was even dominant in one sample (24.06%). More details are given in Graba *et al*. (2013) on the algal composition of the biofilm. The difference between the biofilm algal composition in the two experiments might be due to differences in the seeding sources but more likely due to differences in the physicochemical parameters (temperature and nutrients) because the experiments were run in very different seasons (the first experiment began in mid-January whereas the second experiment began at the end of September).

In the first experiment, other biological measurements (biomass and phytoplankton) only began 2 weeks after *inoculum*, but colonization patterns were recorded using an uncalibrated digital camera from the beginning of the experiments. In the second experiment, upper view images of the artificial cobbles were taken daily through a Plexiglas window in the three sections (HV, IV and LV) using a digital camera (Nikon D1 model, 2000 × 1312 pixel resolution), with constant illumination provided by a flash and a reflective artificial pattern in the camera view used to renormalize the image intensity. Besides, 7 days after *inoculum*, four cobbles were selected randomly in each of the three HV, IV and LV sections, away from the edges, and dried (80 °C, overnight) to obtain the dry weight of biofilm on each hemisphere.

Numerical simulations

Numerical approach. The governing equations for an unsteady incompressible flow with negligible gravitational effects are the Navier–Stokes equations reading

$$\nabla \cdot \mathbf{u} = 0 \tag{1}$$

$$\frac{\partial \mathbf{u}}{\partial t} + \mathbf{u}\nabla\mathbf{u} = -\frac{1}{\rho}\nabla p + \nu \ \nabla \cdot \left[\nabla\mathbf{u} + (\nabla\mathbf{u})^T\right] \tag{2}$$

where $\mathbf{u}$ denotes fluid velocity, p pressure, ρ density and ν kinematic viscosity of the fluid (ρ and ν are constant throughout the present work). The spatial discretization of Equations 1 and 2 is made on a Cartesian, three-dimensional, orthogonal structured mesh. The discretization makes use of a staggered grid, and Equations 1 and 2 are integrated in space using a finite-volume method with second-order accuracy. The time-advancement algorithm used in the JADIM code has been described in details by Calmet (1995). Briefly, a mixed third-order Runge–Kutta/Crank–Nicolson scheme is used to compute advective and viscous terms while incompressibility is satisfied at the end of each time step via a projection method for which a Poisson equation is solved.

In the JADIM code is implemented an IBM based on the method proposed by Yuki *et al*. (2007). This method employs a body force proportional to a solid volume fraction for coupling the solid and the fluid. It allows for the simulation of high-Reynolds-number flows in the presence of fixed or moving objects of arbitrary shape. Here, the immersed boundary is defined by the volume fraction of the solid denoted α, which is equal to 1 if the cell is completely in the object and 0 otherwise, and $0<\alpha<1$ if the cell is crossed by the immersed boundary. The expression of α depends on the shape of the object. Here, a hyperbolic-tangent function is used as a surface digitizer for computing the volume fraction. The detailed calculation of α used in the present work can be found in Yuki *et al*. (2007). In the present case, we assume a no-permeability and no-slip condition at the motionless immersed boundaries (representing the cobbles), so the mass and momentum equations can be written in the new form

$$\nabla\cdot\mathbf{u} = 0 \tag{3}$$

$$\frac{\partial\mathbf{u}}{\partial t} = -\nabla P + H + f \tag{4}$$

$$H = -\mathbf{u}\nabla\mathbf{u} + \nu\ \nabla\cdot\left[\nabla\mathbf{u} + (\nabla\mathbf{u})^T\right] \tag{5}$$

where $P = \frac{p}{\rho}$ and $\nu = \mu/\rho$. Note that Equations 4 and 5 are similar to the Navier–Stokes equation 2 with the exception of the last (body force) term f. This new term allows to modify the velocity field so as to take into account the presence of the immersed boundary. The simplified time-advancement scheme for $\mathbf{u}$ between time $t = n\Delta t$ and $t = (n+1)\Delta t$, n being the time increment and Δt the time step, is the following.

We first calculate a fluid predictor velocity $\widetilde{\mathbf{u}}$

$$\widetilde{\mathbf{u}} = \mathbf{u}^n + \Delta\mathrm{t}(-\nabla P^n + H^n) \tag{6}$$

We then compute the body force f as

$$f = -\alpha\widetilde{\mathbf{u}}/\Delta\mathrm{t} \tag{7}$$

and update the fluid predictor velocity by

$$\widetilde{\mathbf{u}}^{n+1} = \widetilde{\mathbf{u}} + \Delta t f \tag{8}$$

Note that for cells inside the solid hemispheres, $\alpha = 1$; thus, according to Equations 7 and 8, $f = -\widetilde{\mathbf{u}}/\Delta\mathrm{t}$ and $\widetilde{\mathbf{u}}^{n+1} = 0$, so as expected, there is no motion inside the hemisphere. For cells far from the hemispheres, $f = 0$, so the velocity field is unaffected by the immersed objects. Finally, the projection method is applied in order to obtain the new velocity field $\mathbf{u}^{n+1}$ satisfying the incompressibility constraint, $\mathbf{u}^{n+1}$ being obtained from $\widetilde{\mathbf{u}}^{n+1}$.

Numerical setup. Before performing numerical simulations with the same conditions as for the two experiments, the numerical approach was validated in a configuration similar to that investigated here, namely a rough turbulent boundary layer over a bed of cubes. The results were compared with those obtained with a different method by Coceal *et al*. (2006). This corresponds to a turbulent Reynolds number Re_t based on the height h of the cubes and the friction velocity u_p^* of $Re_t = u_p^* h/\nu = 500$. The friction velocity u_p^* used here is based upon the constant pressure gradient $\partial P/\partial x$ chosen for the numerical simulation, defined by $\partial P/\partial x = -\rho u_p^{*2}/D$, where D is the height of the domain. This pressure gradient is imposed along the streamwise direction in order to ensure the establishment of a fully developed turbulent boundary layer after about $200T$, where $T = h/u_p^*$ is an eddy turnover time (equal to 2.17 s here). Following Coceal *et al*. (2006), the mean turbulent characteristics quantities were then obtained by averaging the next 700 temporal samples with a time interval of T, in order to ensure sufficient statistical convergence. Simulations with different grid resolutions showed that a grid size $\Delta = h/16$ (where h is the cube height) was sufficient to obtain the same results as Coceal *et al*. (2006). Such a grid size roughly corresponds to 8η, where η is an estimated Kolmogorov length scale based upon the value of the maximal mean velocity gradient at the top of the cubes and the friction velocity u_p^*, following the same formula as in Coceal *et al*. (2006) for ε, namely $\varepsilon \approx 2.5 u_p^{*3}/h$. This value of 8η for the grid size was then adopted as a reference to perform simulations of the turbulent boundary layer over a bed of hemispheres in the present study.

Figure 2 shows a plan view and a three-dimensional view of the computational domain used in the different runs of staggered and aligned configurations (the configuration being defined by the flow direction). The bed of the domain is covered by cobbles of radius h, regularly and periodically positioned according to the corresponding experiments. The runs are code named with the same rule as for the experiments. The longitudinal and transverse lengths for the calculation domains were chosen so that the autocorrelation functions for the longitudinal velocity component would drop below 0.15, in order to capture the effect of the largest turbulent structures in the flow (Kim *et al*. 1987).

For all the simulations, periodic boundary conditions are imposed along the streamwise and spanwise directions; a free-slip condition is set at the top of the domain whereas a no-slip boundary condition is imposed at the bottom and on the cobbles. The flow is generated and maintained by a

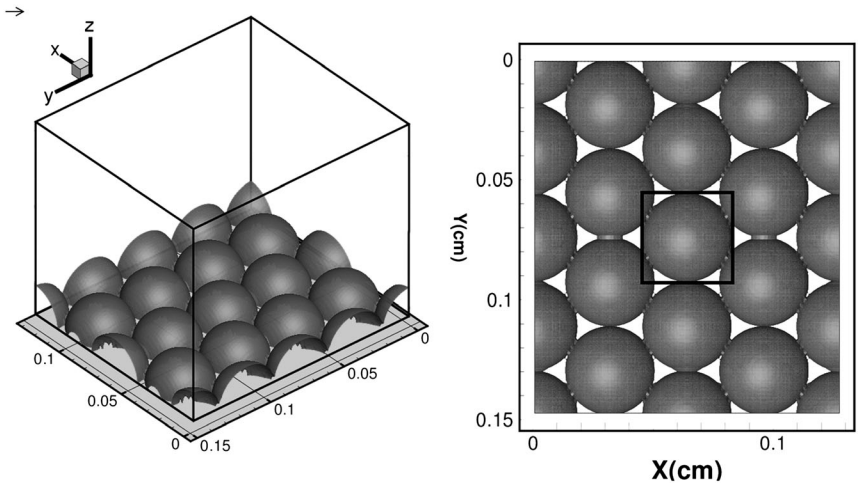

Figure 2. Plan and 3D views of numerical computational domain. The minimal pattern is framed by a square

constant streamwise pressure gradient equal to $-\rho u_p^{*2}/D$. The grid size was chosen in order to capture spatial scales down to 8η (where η is the Kolmogorov scale) above the canopy with at least five points in the free surface boundary layer (following Calmet, 1995), and between 4 and 6η in the canopy.

The colonization patterns were quite similar in the second experiment for IV and HV regions of Moulin *et al*. (2008) and Graba *et al*. (2013). Because a simulation with the same flow parameters as in HV experiment would have been extremely costly, because of high value of the friction velocity, we decided to perform numerical simulations only for LV and IV flows. The confinement was different in the two experiments for IV flows ($IV_{A6.5}$ and $IV_{S4.25}$), so we also performed a run for a staggered configuration with the same confinement as in the first experiment, namely $IV_{S6.5}$, for which no experiments have been performed. This case will be used to discriminate effects of Reynolds number and confinement on the local flow topology. The value of the pressure gradient that drives the flow in the numerical simulations was prescribed by choosing a value of u_p^* equal to the value of the experimental friction velocity u_{exp}^* inferred from measurements in the two experiments (values given in Graba *et al*., 2010, and Moulin *et al*., 2008, respectively), that is, $u_p^* = u_{exp}^*$. All the run parameters are summarized in Table I for the four runs presented in this study, that is, $LV_{S6.5}$, $IV_{S4.25}$, $IV_{S6.5}$ and $IV_{A6.5}$.

Double-averaging method

For turbulent boundary layer flow over a rough surface, the presence of roughness generates a strong inhomogeneity of the flow in the so-called roughness sublayer close to the bed. To cope with this apparent complexity, Raupach *et al*. (1991) introduced a double-averaging procedure that consists in making both a time and a space averaging in the horizontal directions. It was then adopted by many authors to describe rough turbulent boundary layers (Finnigan, 2000; Cheng and Castro, 2002; Pokrajac *et al*., 2007; Mignot *et al*., 2009) and formalized by Nikora *et al*. (2007a) to infer the so-called DANS. In this approach, prognostic variables, ψ, are decomposed into three components, reading

$$\psi\left(\overrightarrow{X},t\right) = \langle\overline{\psi}\rangle(z) + \overline{\psi}\left(\overrightarrow{X}\right) + \psi'\left(\overrightarrow{X},t\right) \tag{9}$$

Applying the double-averaging technique to the velocity component, u_i, gives

$$u_i = U_i + \widetilde{u}_i + u_i'$$

where $U_i(z) = \langle\overline{u_i}\rangle$ is the time and space averaged velocity, referred to here as the double-averaged velocity, $\widetilde{u}_i(x,y,z) = \overline{u}_i - \langle\overline{u}\rangle = \overline{u}_i - U_i(z)$ is the spatial variation of the time mean flow, referred to as the dispersive component, and $u_i'(x,y,z,t) = u_i - U_i - \widetilde{u}_i$ is the turbulent fluctuation. The overline denotes a time average, and the angle brackets denote a spatial average in horizontal directions x and y. As detailed in Nikora *et al*. (2007a), applying time and spatial averaging to the mass and momentum Equations 1 and 2 yields the DANS, valid at any height z and reading

$$\frac{\partial\langle\overline{u_i}\rangle}{\partial x_i} = 0 \tag{10}$$

$$\frac{\partial\langle u_i\rangle}{\partial t} + \langle u_j\rangle\frac{\partial\langle u_i\rangle}{\partial x_j} = -\frac{\partial\langle\overline{P}\rangle}{\partial x_i} + \frac{1}{\rho}\frac{\partial\tau_{ij}}{\partial x_j} + D_i \tag{11}$$

$$\frac{\tau_{ij}}{\rho} = -\left\langle\overline{u_i'u_j'}\right\rangle + \nu\frac{\partial\langle\overline{u_i}\rangle}{\partial x_j} - \langle\widetilde{u}_i\widetilde{u}_j\rangle \tag{12}$$

Table I. Numerical model and runs parameters

Runs	Parameter	Symbol	Value	Units
$LV_{SH6.5}$	Computational grid dimensions	$N_x \times N_y \times N_z$	$88 \times 96 \times 138$	–
	Domain dimensions	$L_x \times L_y \times L_z$	$7h \times 8h \times 6.64h$	m
	Initial duration	–	$200T$	s
	Time samples	N	600	–
	Eddy turnover time	T	2.17	s
	Friction velocity	u_p^*	0.85	cm/s
$IV_{AH6.5}$	Computational grid dimensions	$N_x \times N_y \times N_z$	$144 \times 128 \times 188$	–
	Domain dimensions	$L_x \times L_y \times L_z$	$8h \times 7h \times 6.64h$	m
	Initial duration	–	$100T$	s
	Time samples	N	500	–
	Eddy turnover time	T	0.76	s
	Friction velocity	u_p^*	2.42	cm/s
$IV_{SH6.5}$	Computational grid dimensions	$N_x \times N_y \times N_z$	$140 \times 160 \times 204$	–
	Domain dimensions	$L_x \times L_y \times L_z$	$7h \times 8h \times 6.64h$	m
	Initial duration	–	$100T$	s
	Time samples	N	464	–
	Eddy turnover time	T	0.71	s
	Friction velocity	u_p^*	2.61	cm/s
$IV_{SH4.25}$	Computational grid dimensions	$N_x \times N_y \times N_z$	$128 \times 144 \times 128$	–
	Domain dimensions	$L_x \times L_y \times L_z$	$7h \times 8h \times 4.25h$	m
	Initial duration	–	$100T$	s
	Time samples	N	496	–
	Eddy turnover time	T	0.87	s
	Friction velocity	u_p^*	2.15	cm/s
Common parameters	Kinematic viscosity	ν	1.002×10^{-6}	m^2/s
	Density	ρ	1000	kg/m^3
	Hemisphere radius and height	$\Phi/2$ and h	1.85	cm

$$D_i = \frac{1}{V} \iint_{S_{int}} \overline{P} n_i dS - \frac{1}{V_f} \iint_{S_{int}} \nu \frac{\partial \overline{u_i}}{\partial n} dS \qquad (13)$$

where V_f is the volume occupied by the fluid, S_{int} is the surface area of the obstacles within the averaging volume V, n_i is the unit normal pointing from S_{int} into V_f and ν is the kinematic viscosity. The spatially averaged total stress τ_{13} (or, equivalently, τ_{xz}) is obtained from Equation 12 and contains the usual Reynolds stress $\left\langle \overline{u' w'} \right\rangle$, the viscous stress $\nu \frac{\partial \langle \overline{u} \rangle}{\partial z}$ and the dispersive stress $\langle \widetilde{u}\widetilde{w} \rangle$.

$$\frac{\tau_{13}}{\rho} = -\left\langle \overline{u' w'} \right\rangle + \nu \frac{\partial \langle \overline{u} \rangle}{\partial z} - \langle \widetilde{u}\widetilde{w} \rangle \qquad (14)$$

The dispersive stress represents transport of momentum by spatial variations in the horizontal plane. Within the canopy volume V, the drag term D_i in Equation 13 includes the form drag and the viscous drag.

In the numerical simulations, all the terms of the DANS are available, whereas in experiments, dispersive terms are not always accessible or poorly estimated because of low spatial sampling in the horizontal directions (Florens *et al.*, 2013). In many experimental studies, the turbulent boundary layer is therefore investigated only in the inertial sublayer far above the roughness elements, where dispersive terms are negligible. However, as shown by Castro *et al.* (2006) and Florens (2010), the universal log law for the turbulent boundary layer extends far inside the roughness sublayer and may even exist only there in very confined flows.

RESULTS

Turbulent boundary layer above the hemispheres

Friction velocity for the log law. Direct comparison of the double-averaged vertical profiles for the flow conditions of $LV_{S6.5}$ obtained in the second experiment (PIV measurements) and the numerical simulation reveals that the values are systematically larger in the experiment than those in the simulation. The reason for this discrepancy is due to an inappropriate tuning of the pressure gradient in the numerical simulations. As pointed out by Florens (2010), the friction velocity that scales the log law in a confined flow is different from the friction velocity that could be inferred from the wall shear stress τ_p. Because the pressure drag in the numerical simulations is directly related to the wall shear stress, the friction velocity u_p^* is different from the velocity scaling for the log law (noted u_{exp}^* in the experiments).

Following the conclusion of Florens (2010) that the right friction velocity scale for the vertical profiles of flow statistics is given by the value of the total stress τ_{13} at the top of the canopy (or linearly extrapolated to $z=h$), we chose to scale all the flow statistics by this value, named $u^*_{z=h}$ from now. Following Florens (2010), the value of $u^*_{z=h}$ is deduced from u^*_p by the formula $u^*_{z=h} = u^*_p(1-h/D)$. With this scaling, dimensionless profiles for the numerical simulations get closer to those of the experiment (Figure 3), but a small discrepancy persists. Indeed, the value of the friction velocity inferred from laser Doppler velocimetry (LDV) or PIV measurements in the two experiments (Moulin *et al*., 2008; Graba *et al*., 2010) was taken as the value of the Reynolds stress $<\overline{u'w'}>$ alone, following the conclusions of Castro *et al*. (2006). Because the vertical profiles of $<\overline{u'w'}>$ are linear in the upper part of the flow and weakly curved near the top of the hemispheres (Figure 3), the contribution of the dispersive stress would yield larger values of the total shear stress τ_{13}, larger than $<\overline{u'w'}>$ at $z=h$. Linear extrapolations of the vertical profiles of $<\overline{u'w'}>$ at $z=h$ were then used to estimate $u^*_{z=h}$ from the experimental measurements, leading to a 15% increase of the actual friction velocity (i.e. $u^*_{z=h} \approx 1.15 u^*_{exp}$). The relevance of this new estimation method is demonstrated by the collapse of dimensionless flow statistics for the experiments and the numerical simulations in Figure 3.

Log law parameters. As shown by Florens (2010), a log law persists even for confined flows over a rough bed, as long as the vertical profiles of double-averaged mean longitudinal velocity $<\overline{u}>$ are considered, which reads

$$\frac{<\overline{u}>}{u^*} = \frac{1}{\kappa} ln\left(\frac{z-d}{z_0}\right) = \frac{1}{\kappa} ln\left(\frac{z-d}{k_s}\right) + 8.5$$

where $\kappa = 0.41$ is the Karman constant, d the displacement height, z_0 the roughness length, k_s the equivalent hydraulic roughness related to z_0 by the simple relation $k_s = z_0 exp(8.5\kappa) \approx 32 z_0$ and u^* the relevant friction velocity, that is, $u^* = u^*_{z=h}$ as discussed earlier.

Vertical profiles of double-averaged longitudinal velocity $<\overline{u}>$ in the numerical simulations were used to calculate these log law parameters. Firstly, the quantity $exp(\kappa <\overline{u}> /u^*)$ was plotted as a function of z to determine the range of validity of the log law behaviour $<\overline{u}> /u^*$. A linear regression was then performed on the validity range to calculate d and z_0 because $exp(\kappa <\overline{u}> /u^*) = (z-d)/z_0$. As observed by Florens (2010), the validity range begins just above the top of the hemispheres, $z=h$, and extends through the roughness sublayer up to $z = 1.3-1.4h$, depending on the confinement. Values for the log law validity range and log law parameters are given in Table II for the numerical simulations, along with values inferred

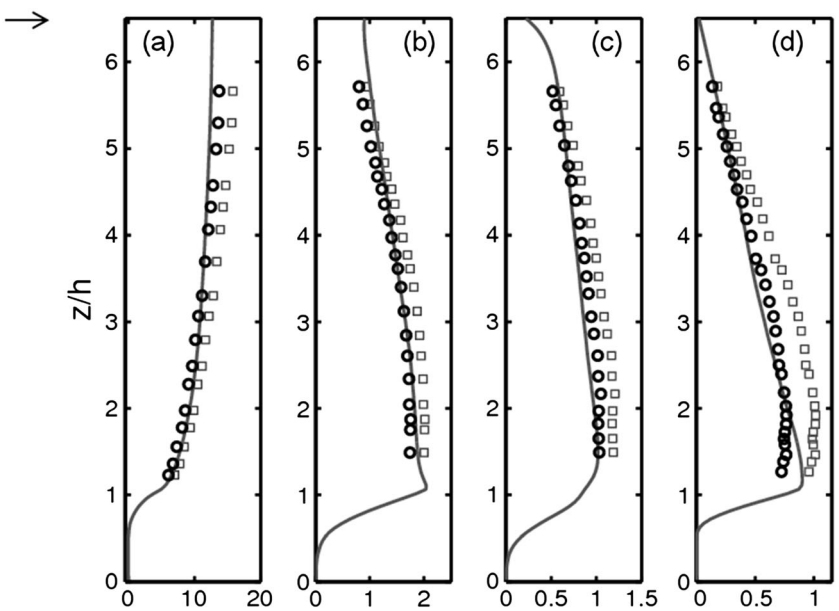

Figure 3. Comparison of numerical and experimental results for $LV_{S6.5}$. Vertical profiles of (a) the double averaging longitudinal velocity $<\overline{u}>$, (b) the RMS of streamwise velocity $\sqrt{<\overline{u'^2}>}$, (c) the RMS of vertical velocity $\sqrt{<\overline{w'^2}>}$ and (d) the Reynolds stress $<\overline{u'w'}>$. Experimental data normalized by u^*_{exp} or u^{*2}_{exp} (squares □); experimental data normalized by $1.15u^*_{exp}$ or $\left(1.15u^*_{exp}\right)^2$ (because $u^*_{z=h} \approx 1.14 u^*_{exp}$, see text) (circles o); numerical data normalized by $u^*_{z=h}$ or $u^{*2}_{z=h}$ (solids lines –)

Table II. Comparison of the log law parameters for the turbulent boundary layer in numerical simulations and experiments

Flow type	Log law parameters	Numerical simulation	Experiment
$LV_{S6.5}$	u_p^* (cm/s)	0.86	–
	u_{exp}^* (cm/s)	–	0.85
	$u_{z=h}^*$ (cm/s)	0.79	–
	z_{LogLaw}^{up}/h	1.21	1.54
	d/h	0.88	0.81
	z_0/h	0.025	0.020
	k_s/h	0.80	0.63
$IV_{A6.5}$	u_p^* (cm/s)	2.4	–
	u_{exp}^* (cm/s)	–	2.8
	$u_{z=h}^*$ (cm/s)	2.2	–
	z_{LogLaw}^{up}/h	1.56	1.3
	d/h	0.84	0.56
	z_0/h	0.021	0.055
	k_s/h	0.68	1.74
$IV_{S6.5}$	u_p^* (cm/s)	2.6	–
	u_{exp}^* (cm/s)	–	–
	$u_{z=h}^*$ (cm/s)	2.4	–
	z_{LogLaw}^{up}/h	1.16	–
	d/h	0.87	–
	z_0/h	0.022	–
	k_s/h	0.70	–
$IV_{S4.25}$	u_p^* (cm/s)	2.1	–
	u_{exp}^* (cm/s)	–	2.61
	$u_{z=h}^*$ (cm/s)	1.9	–
	z_{LogLaw}^{up}/h	1.17	1.32
	d/h	0.88	0.76
	z_0/h	0.022	0.025
	k_s/h	0.72	0.79

Experimental values are those cited in Graba *et al*. (2010) for the first experiment (aligned configuration) and Moulin *et al*. (2008) for the second experiment (staggered configuration). Upper limit of log law validation range z_{LogLaw}^{up}, displacement height d, roughness length z_0 and friction velocity $u_{z=h}^*$. u_{exp}^* is the value of friction velocity cited in Graba *et al*. (2010) and Moulin *et al*. (2008).

from experimental measurements as given by Graba *et al*. (2010) and Moulin *et al*. (2008).

As for log law parameters, the largest discrepancy between experimental and numerical results is found for the $IV_{A6.5}$ flow regime. For this configuration, flow measurements were performed by LDV, but as indicated in Graba *et al*. (2010), the friction velocity was inferred from the profiles of u_{rms} instead of the profiles of $<\overline{u'w'}>$, and the values of the log law parameters are quite sensitive to the choice of u^* for the linear regression and to the spatial resolution of measurements in the log law region. Indeed, in Graba *et al*. (2010), the values of d and z_0 9 days after *inoculum* are closer to the results from the numerical simulation, with the values of d/h and z_0/h equal to 0.71 and 0.032, respectively. Because the biofilm is not developed enough to strongly modify the turbulent boundary layer, these values obtained with the profiles of $<\overline{u'w'}>$ may be more relevant for comparison with numerical results. For experiments with PIV measurements, the accordance with the values inferred from the numerical simulations is far better. We shall come back to this point in the discussion section.

Three-dimensional flow topology near the hemispheres

Mean velocity field in the roughness sublayer. The three-dimensional topology of the mean flow components $\overline{u}$, $\overline{v}$ and $\overline{w}$ is completely different for the staggered and aligned configurations. Horizontal cross-sections at $z = h/2$ and vertical cross-sections in the midplane of a hemisphere have been plotted in Figures 4 and 5 to illustrate the most striking features of the three-dimensional flow.

In the aligned configuration, high longitudinal velocities are found along alleys at around $y/h = \pm\sqrt{3}/2 \approx \pm 0.9$, which correspond to the half distance between hemisphere alignments (Figure 4a). A recirculation vortex forms in the rear of the hemisphere, taking shape of a horseshoe vortex, whose vertical cross-section yields the vortex cores visible in Figure 4a at ($x/h = 0.9, y/h = \pm 0.25$) and in Figure 5a at ($x/h = 1.1, z/h = 0.85$).

In the staggered configuration (Figures 4b–d and 5b–d), there are no more preferential alleys for the flow between the hemispheres, and fluid particles have to meander between successive hemispheres. The impingement of flow in front of each hemisphere generates a stagnation point whose vertical position is easily deduced from Figure 5b–d. The flow topology at the rear of the hemisphere is less obvious than that in the aligned configuration. Indeed, some recirculation occurs between two successive hemispheres, limited laterally by the meandering of the high-velocity flow region. This recirculation is formed by the downward motion at the front of the hemisphere, below the stagnation point [Figure 5b–d, around ($x/h = -1, z/h = 0.5$)], and joins an upward motion at the rear of the hemisphere located upstream [Figure 5b–d, around ($x/h = +1, z/h = 0.7$)]. This upward motion detaches from the rear of the hemisphere just before reaching its top. This detachment, associated with the detachment of flow at the top of the hemisphere, generates a very small low velocity region just behind the top of the hemisphere [Figure 5b–d, around ($x/h = +0.6, z/h = 0.9$)]. In vertical planes away from the midplane plotted in Figure 5b–d, the near-top low velocity region moves gradually downward, forming a crown at the rear of the hemisphere.

Flow conditions close to the hemispheres. To investigate the imprint of this flow topology near the hemispheres, the radial gradient of mean tangential velocity was calculated by (i) interpolating in spherical coordinates (r, θ, φ) the mean velocity flow components obtained on the Cartesian grid, (ii) calculating the mean tangential components $\overline{u_\theta}$ and $\overline{u_\phi}$, and

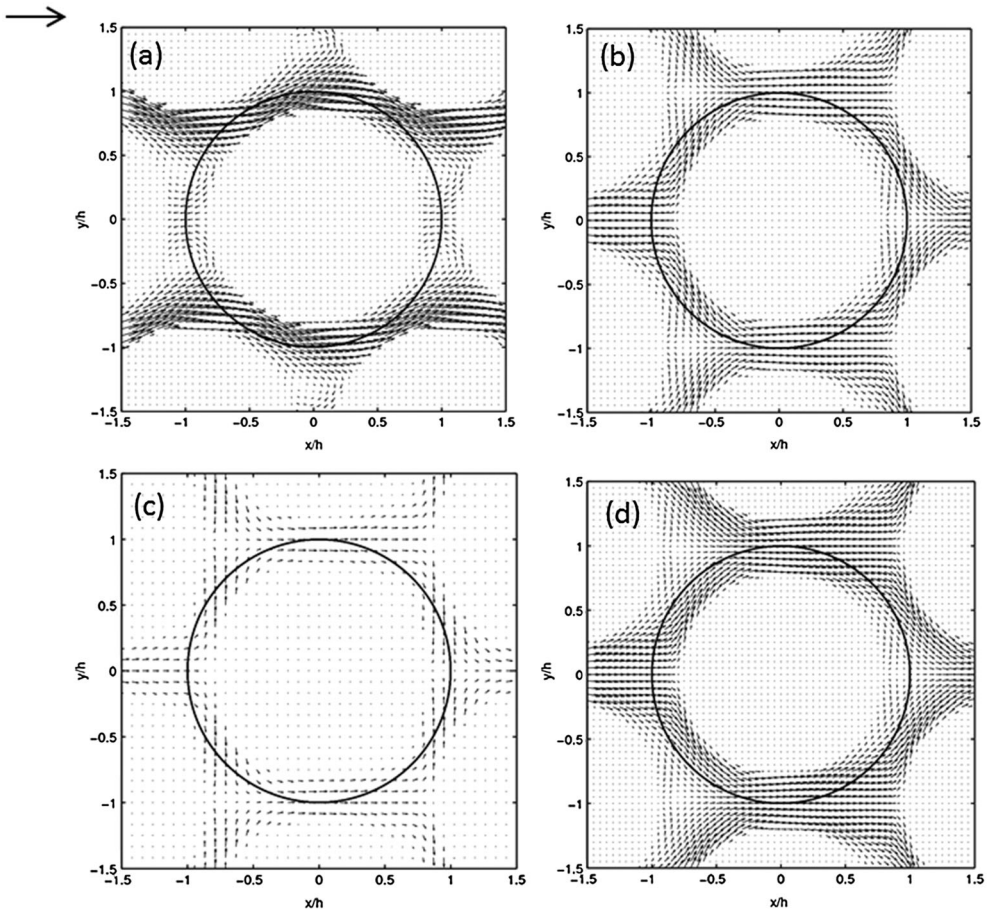

Figure 4. Mean horizontal velocity field ($\overline{u}$, $\overline{v}$) in a horizontal plane located at $z/h = 0.5$ for (a) $IV_{A6.5}$, (b) $IV_{S6.5}$, (c) $LV_{S6.5}$ and (d) $IV_{S4.25}$. The velocity components have been non-dimensionalized by the friction velocity $u^*_{z=h}$

(iii) performing a linear regression on the three closest points to the hemisphere, located at $r/h = 1.05$, $r/h = 1.10$ and $r/h = 1.15$, respectively (adding a zero velocity condition on the hemisphere surface at $r/h = 1$). This method yields an accurate estimate for the radial derivative of the mean tangential velocity $\mathbf{u_{tr}} = \partial\left(\overline{u_\theta}\mathbf{e}_\theta + \overline{u_\phi}\mathbf{e}_\phi\right)/\partial r$, the norm of which will be referred to as mean local velocity gradient u_{rt} defined by $u_{rt} = \| \mathbf{u_{tr}} \|$. In this region close to the hemisphere, the components of the turbulent stress tensor $\overline{u'_i u'_j}$ were far smaller than the viscous shear stress, so that this mean local velocity gradient u_{rt} is directly related to the total local shear stress on the hemispheres τ by $\tau = \mu u_{rt}$.

Top views of the distribution of tangential velocity shear for aligned and staggered configurations are plotted in Figure 6. In the aligned configuration (Figure 6a), the imprint of the horseshoe recirculating vortex generates indeed two symmetric stagnation points at the front of the hemisphere, located around ($x/h = -0.7$, $y/h = \pm 0.5$) in Figure 6a, linked together by a low shear stress line that crosses the vertical midplane around $x/h = -0.6$, visible also around ($x/h = -0.6$, $z/h = 0.85$) in Figure 5a. The imprint at the rear of the hemispheres takes the form of a low shear stress region with less contrasted conditions than that at the front of the hemisphere. In the staggered configuration (Figure 6b–d), the stagnation point at the front is clearly put in evidence (at $x/h = -0.7$, $y/h = 0$), while the low velocity region at the rear of the hemisphere generates a crown-like pattern on the hemisphere.

Contours of the mean local shear stress τ ($= \mu u_{rt}$), normalized by $\mu u^*_{z=h}/h$, have been plotted in Figure 7 in grey levels. The stagnation points and low shear stress regions are easily identified in these figures. For staggered configurations (Figure 7b–d), the patterns are almost identical for $IV_{S4.25}$ and $IV_{S6.5}$, whereas for $LV_{S6.5}$, the low shear region at the rear, associated with the upward motions due to the recirculation flow, is wider.

Colonization patterns

In the first experiment with aligned hemispheres, a very regular and homogenous colonization pattern could be

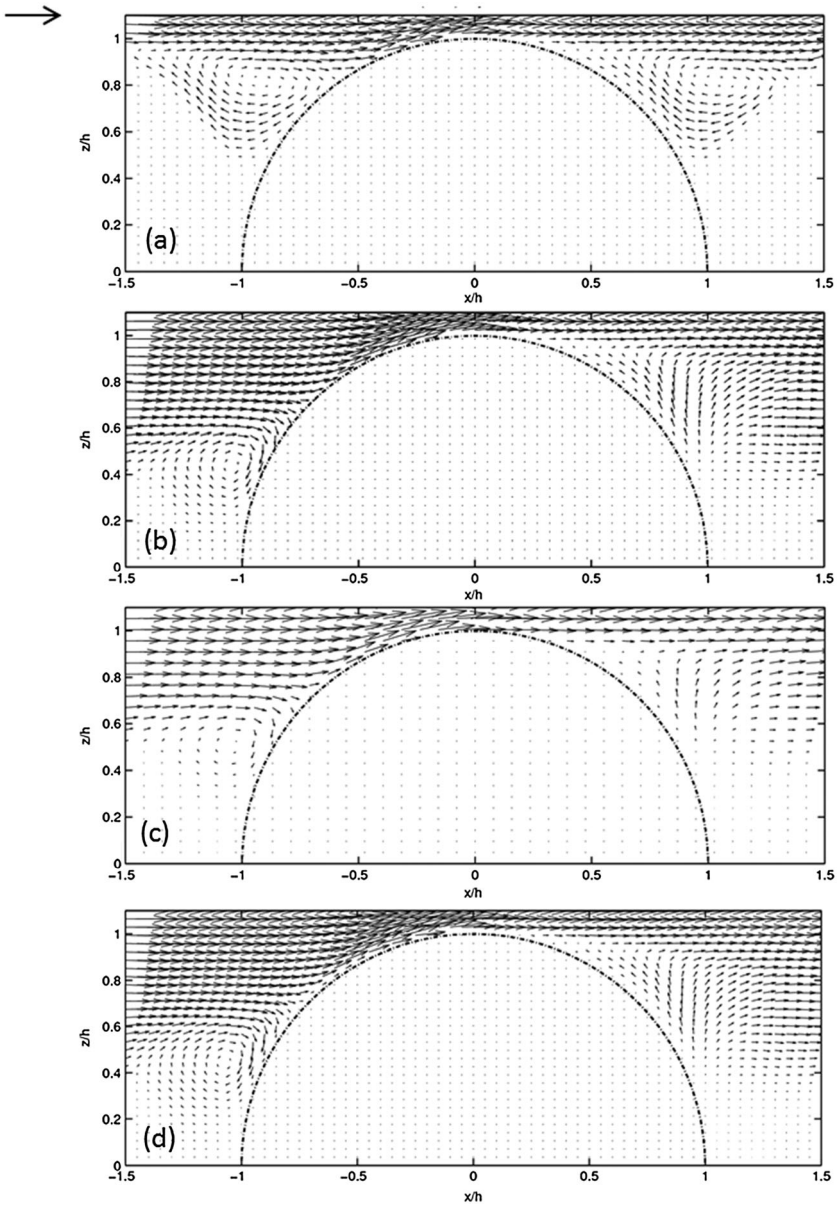

Figure 5. Mean velocity field ($\overline{u}$, $\overline{w}$) in the vertical midplane located at $y/h = 0$ for (a) $IV_{A6.5}$, (b) $IV_{S6.5}$, (c) $LV_{S6.5}$ and (d) $IV_{S4.25}$. The velocity components have been non-dimensionalized by the friction velocity $u^*_{z=h}$

observed on the artificial cobbles (Figure 8): initial patches located around two symmetric points in the front side of the hemisphere, followed by a thin line between them, before the biofilm spread over the whole hemisphere. The location of the two symmetric points corresponds to the two stagnation points identified in the near surface flow in Figure 6a. In the second experiment with staggered hemispheres, regular colonization patterns were also observed in all sections (Figure 9). For all flow conditions, an initial patch of biofilm was found at the front of the hemispheres, corresponding to the stagnation point identified in the near surface flow in Figure 6b–d. In the low velocity region $LV_{S6.5}$, an additional patch was also found at the rear of the hemisphere, taking a half-crown shape that corresponds to the rear low shear region also visible in Figure 6c and discussed earlier. This patch was not observed in the $IV_{S4.25}$ and $HV_{S2.5}$ flows.

In the second experiment, a spatial averaging of the colonization pattern at day 5 was performed, by taking the complete available hemispheres of Figure 9, subtracting the image without biofilm taken at day 0 and selecting the image of the red channel (one of the three channels for color image coding using Red-Green-Blue (RGB) decomposition) where the biofilm contrast was higher. Results are plotted in

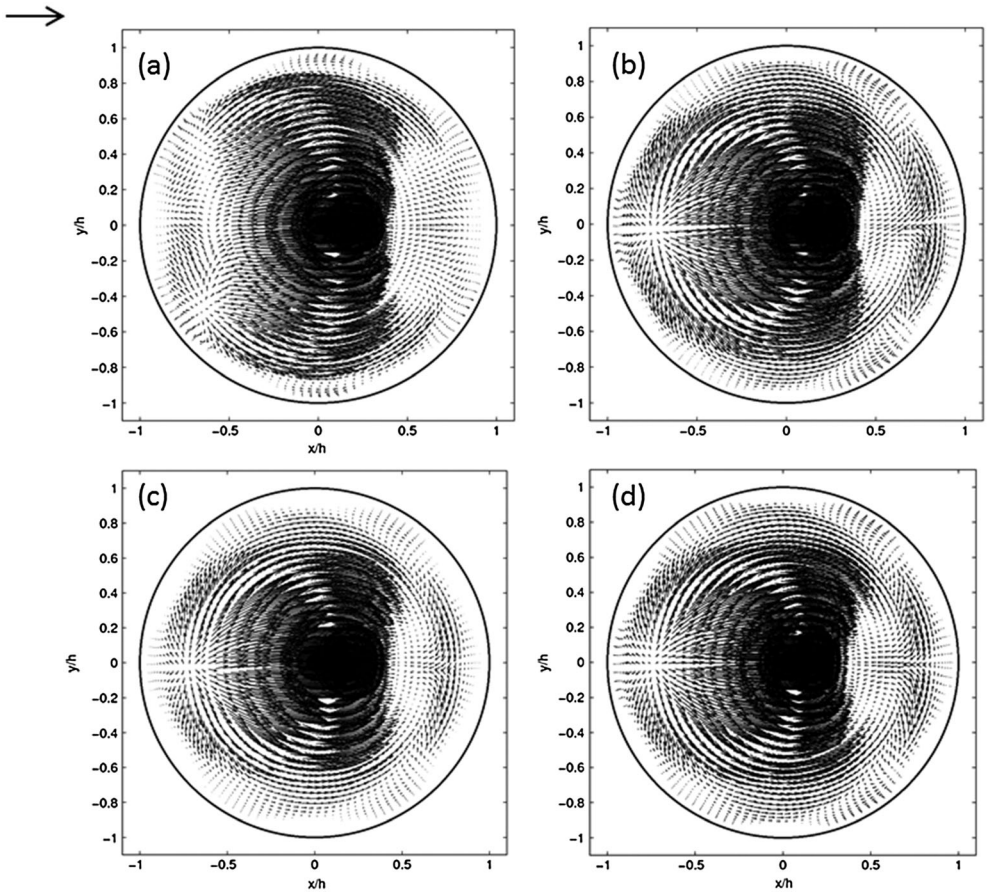

Figure 6. Top view of the mean tangential velocity gradient on an hemisphere for (a) $IV_{A6.5}$, (b) $IV_{S6.5}$, (c) $LV_{S6.5}$ and (d) $IV_{S4.25}$. The velocity gradient components have been non-dimensionalized by $u^*_{z=h}/h$

the upper part of Figure 10, where the colonization patterns are clearly put in evidence. The colonization patch near the front stagnation point occupies an area at day 5 that decreases with increasing friction velocity. The crown-like shape of the rear colonization patch for $LV_{S6.5}$ is obvious, whereas few biofilm seems to accumulate at the rear for $IV_{S4.25}$ and $HV_{S2.75}$ flow regions.

The most colonized parts of the hemispheres were found to correspond to the same maximal level of intensity regions in the three colour channels for the three regions. Nude parts (without biofilm) were associated with intensities close to zero. Choosing the red channel (with best contrast) and applying a threshold at around 25% of the maximal intensity, colonized regions could be extracted and plotted in the lower part of Figure 9. An estimate of the colonized surface on the hemisphere was then calculated by integrating the intensity level with a weighting function $1/\sqrt{1-(r/R)^2}$ (to take into account the projection of surfaces on the top view) on a centred disc with $0 < r/R < 0.95$. Results of this integration are given in Table III, and they reflect the hemisphere surface occupied by the biofilm. The surface of the hemisphere is equal to $2\pi R^2 = 23.25$ cm^2 with R as the geometric mean of the radius $\Phi/2$ and height h of the hemispheres, that is, $R = \sqrt{(\Phi/2)\tilde{n}h}$. In Table III, these occupied surface estimations for day 5 are given, along with dry mass measurements performed at day 7. While the occupied surface estimate somewhat depends on the choice of the intensity threshold (tested for values between 15% and 35% of the maximal intensity), the relative ratio of occupied surface, taking experiment $LV_{S6.5}$ as a reference, is found to be roughly insensitive to the intensity threshold. In addition, the relative area occupied by the biofilm is observed to be in very good accordance with the relative ratio of dry biomass. This supports the idea that biofilm is homogeneously distributed within the colonization pattern and that the biofilm 'thickness' is constant at the early times of initial growth.

DISCUSSION

A first comparison between experimental and numerical results for the structure of the turbulent boundary layer above

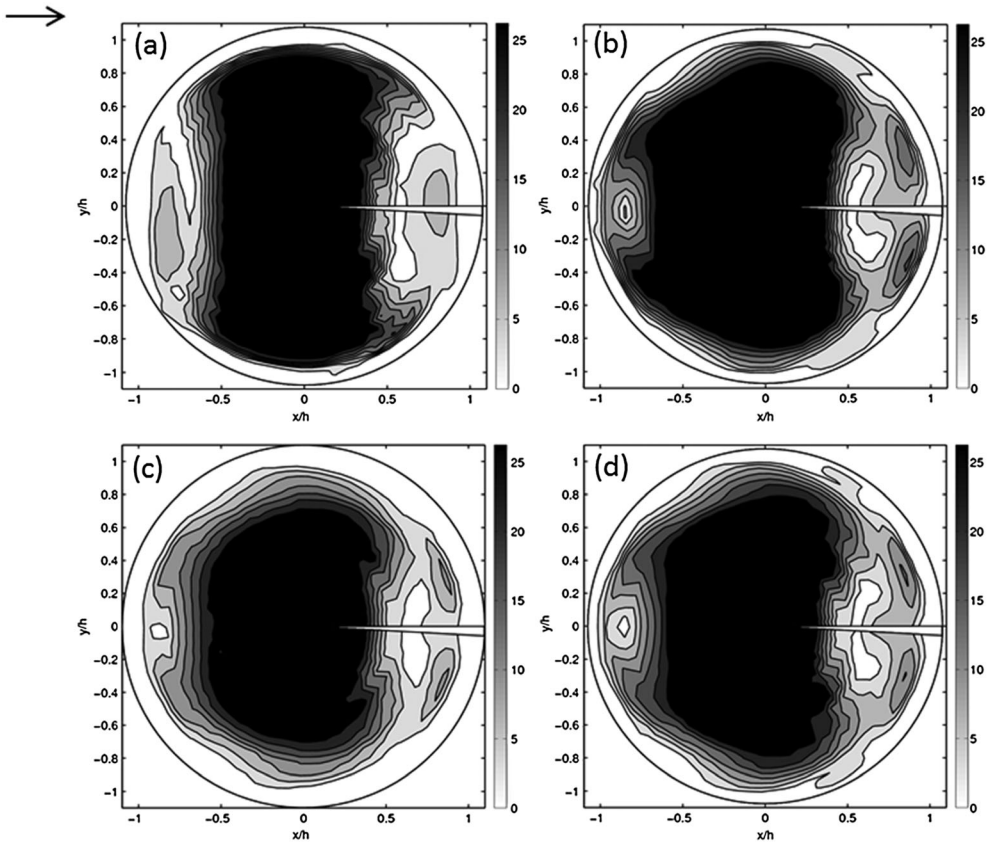

Figure 7. Top view of the isovalues of the mean local shear stress τ on a hemisphere for (a) $IV_{A6.5}$, (b) $IV_{S6.5}$, (c) $LV_{S6.5}$ and (d) $IV_{S4.25}$. The values of the mean shear stress have been non-dimensionalized by $\mu u^*_{z=h}/h$

the canopy (i.e. for $z > h$) for staggered and aligned configurations can be performed by analysing the values of the log law parameters given in Table II (z^{up}_{LogLaw}, d, z_0, k_s). For staggered configurations with the same aspect ratio in the experiments and the numerical simulations, that is, $IV_{S6.5}$ and $IV_{S4.25}$, the values for these parameters are close and in accordance with what is expected from literature for such dense canopies, that is, d/h between 0.75 and 1.0, and k_s/h around unity (here, $0.7 \leq k_s/h \leq 0.8$). For the aligned configuration, values found for the log law parameters in the numerical simulation are different from the parameters given in the experimental study of Graba *et al*. (2010) at the beginning of the experiment. Indeed, the value of the friction velocity at the beginning of the experiment presented in Graba *et al*. (2010) was inferred from an exponential fit applied to vertical profiles of u_{rms}, following Nezu and Nakagawa (1993), and could have been over-estimated, leading to biassed values for k_s and d. Measurements at days

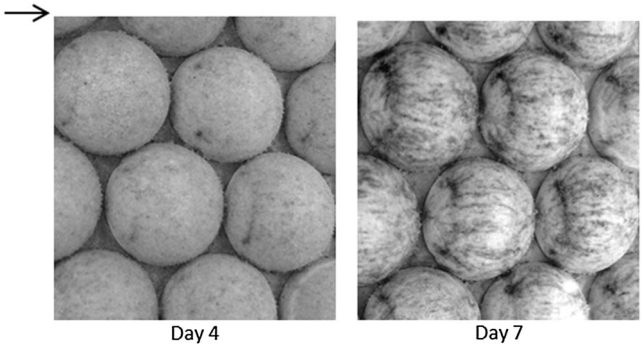

Figure 8. Top view of the biofilm pattern on hemispheres in the first experiment $IV_{A6.5}$ 4 days (left) and 7 days (right) after *inoculum*

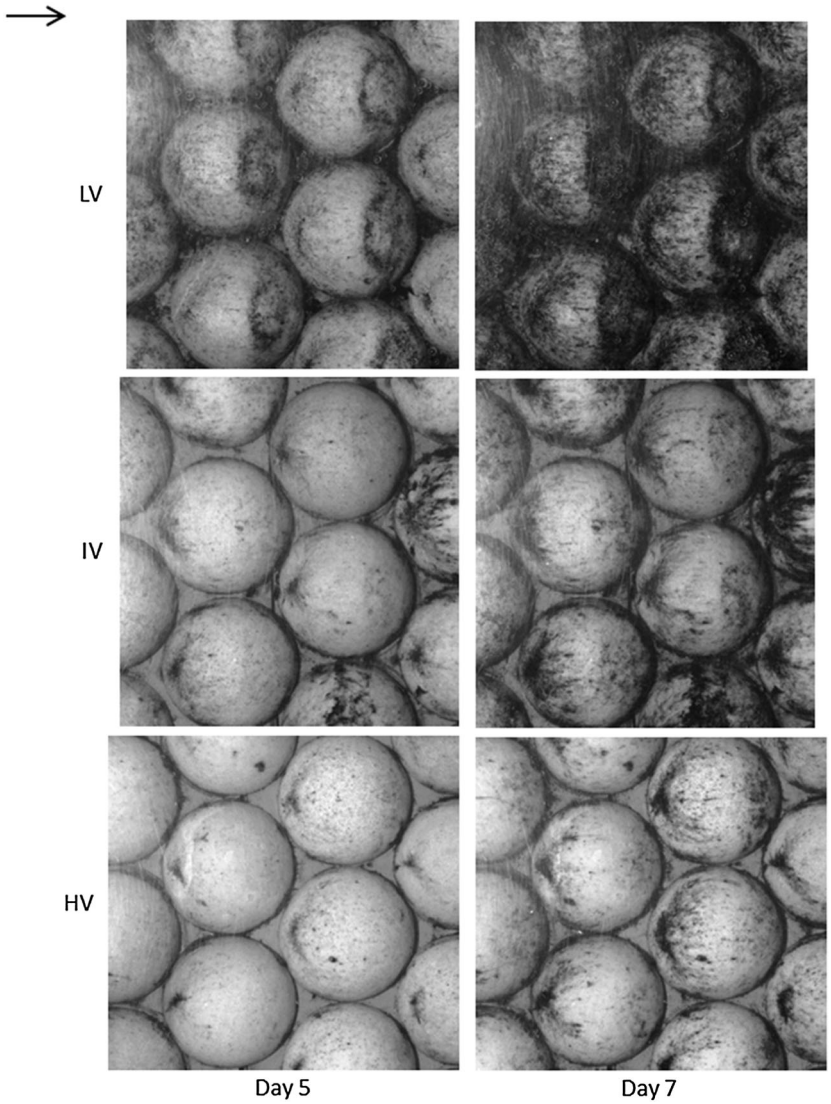

Figure 9. Top view of the biofilm pattern on hemispheres in the second experiment $LV_{S6.5}$ (top), $IV_{S4.25}$ (middle) and $HV_{S2.75}$ (bottom) 5 days (left) and 7 days (right) after *inoculum*

9 and 15 in this experimental work yield values of k_s/h and d/h in the range $k_s/h = [0.69 - 1.01]$ and $d/h = [0.71 - 0.87]$, respectively. While biofilm has already begun to grow at this moment, the numerical simulation yields values of $k_s/h = 0.68$ and $d/h = 0.84$ that are in better agreement with these later experimental results. Of course, the near-hemisphere flow topology is different in the roughness sublayer for staggered or aligned configurations, with a mutual sheltering effect more efficient in the aligned configuration. Yet, both the mixing length and the pressure drag force [see the left term of Equation 13] are expected to remain similar between the two arrangements, thus leading to comparable values of d/h and k_s/h. This is indeed verified in the numerical simulations (see, e.g. the values of k_s and d for runs $IV_{A6.5}$ and $IV_{S6.5}$ in Table II).

The influence of the Reynolds number on the log law parameters can be investigated by comparing numerical simulations with the same bed configuration and the same confinement. Comparing $LV_{S6.5}$ and $IV_{S6.5}$, with roughness Reynolds numbers $k_s^+ = u^* k_s/\nu$ equal to 216 and 575, respectively, [that correspond to fully turbulent boundary layers ($k_s^+ > 70$)] shows that there is a slight but noticeable difference in the value of k_s [i.e. $k_s/h = 0.8(0.7)$ for $k_s^+ = 216(575)$]. This difference is due to a weak modification of the near-hemisphere topology and the associated pressure drag. Although viscous drag [see the right term of Equation 13] should be also different for the two numerical simulations, it is negligible in comparison with the pressure drag because values of k_s^+ are large. The same Reynolds dependence of the flow topology behind a

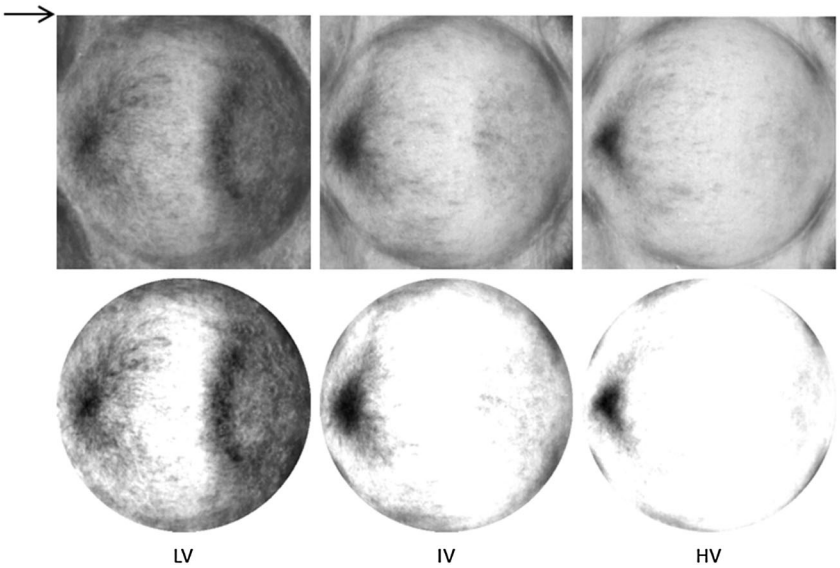

Figure 10. Colonization patterns for LV, IV and HV (from left to right) sections in the second experiment. Top figures are the raw result, and bottom figures are the results after a threshold filtering to capture the biofilm location (see text)

sphere in a uniform flow is observed and explains why the drag coefficient C_D also depends on the Reynolds number. This C_D dependence with Reynolds number would then yield to different values of k_s in a 1D vertical modelling of the velocity profiles in the roughness sublayer (see Macdonald, 2000, for such modelling).

The influence of the confinement on the parameters of the log law can be investigated by comparing numerical simulations with the same bed configuration and turbulent Reynolds number but with varying confinement D/h. Comparing $IV_{S6.5}$ and $IV_{S4.25}$ (which correspond to similar values of k_s^+, respectively, 470 and 575) does not reveal any significant difference between the two confinements. Florens (2010) showed that for a turbulent flow over an array of cubes, confinement becomes significant for values of $h/D > 0.33$ (or, equivalently, $k_s/D > 0.17$) for which a slight decrease of k_s/h is expected while d/h remains constant. Here, $h/D \approx 0.15$ and 0.23 for $IV_{S6.5}$ and $IV_{S4.25}$, respectively. The confinement used in the experiments and numerical simulations presented in this study is lower than the critical value of 0.33, so we expect the log law parameters to be independent of confinement. This is clearly visible in the results of Table II.

Table III. Comparison of dry biomass (measured on day 7) and biofilm patch surface (estimated on day 5 by image processing) for the three flow regions of the second experiment

Flow type	Biofilm dry biomass(mg)	Relative biofilm dry biomass(-)	Biofilm occupied area(cm^2)	Relative biofilm occupied area(-)
$LV_{S6.5}$	16.1 ± 3.9	1	5.35	1
$IV_{S4.25}$	3.9 ± 1.5	0.281 ± 0.16	1.65	0.31
$HV_{S2.75}$	1.5 ± 0.5	0.107 ± 0.057	0.49	0.091

The surface of a hemisphere is equal to 23.25 cm^2.

All the results obtained from the analysis of the turbulent boundary layer developing over two bed configurations for different confinements and bulk velocities can be extended to the flow topology inside the canopy region (i.e. $z/h < 1$). In Figures 4 and 5, it becomes apparent that the flow topology, non-dimensionalized by u^*, strongly depends on the hemisphere arrangement but remains roughly similar for the various flow regimes and confinements. This statement only holds for the flow pattern away from the solid boundaries; close to the solid boundaries, boundary layers develop, whose thickness depends strongly on the flow regimes. As a consequence, this leads to different intensities of the mean local shear stress τ, even when non-dimensionalized by $u^*_{z=h}/h$, as put in evidence in Figure 7 where isovalues of τ get closer as $Re_t = u^* h/\nu$ increases.

The dependence of the dimensionless mean local shear stress on the solid boundaries is of particular importance for the biofilm colonization and early growth dynamics, because its ability to remain attached and grow on the hemispheres is challenged by the local flow conditions. For a boundary layer developing along a flat plate, laws for the friction coefficient $C_f = 2\tau/\left(\rho U_{ext}^2\right)$ (where U_{ext} is the external flow velocity) read $C_f = 0.664 Re_x^{(-1/2)}$ and $C_f = 0.0574 Re_x^{(-1/5)}$ for laminar and turbulent flows, respectively (where $Re_x = U_{ext} x/\nu$). Deep inside the canopy, the external flow for the boundary layer developing along the

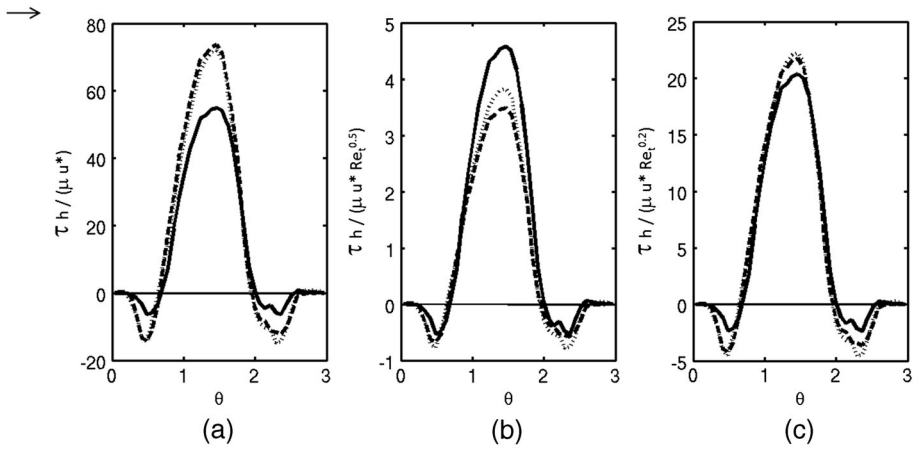

Figure 11. Profile of the mean local shear stress τ on the hemisphere along the vertical midplane $y/h = 0$, for various scalings and flow regimes. $\theta = 0$ (π) corresponds to the front (back) of the hemisphere. τ is scaled by (a) uu^*/h, (b) $\mu u^* Re_t^{0.5}/h$ and (c) $\mu u^* Re_t^{0.2}/h$, respectively. The flow regimes are $LV_{S6.5}$ (solid line), $IV_{S6.5}$ (dashed line) and $IV_{S4.25}$ (dotted line), respectively

hemispheres scales as u^*, and the corresponding laws for the local shear stress would read $\tau/(\mu u^*/h) = 0.332 Re_t^{1/2}$ and $\tau/(\mu u^*/h) = 0.0287 Re_t^{4/5}$, respectively. However, because the colonization begins around stagnation points in the experiments, a more appropriate flow model would be the flow around a stagnation point. For laminar flows, the law for the friction coefficient leads to the same kind of scaling for $\tau/(\mu u^*/h)$, namely $\tau/(\mu u^*/h) \approx Re_t^{1/2}$. For a turbulent laminar boundary layer around a stagnation point, the shear distribution depends very strongly on the turbulence intensity of the incident free stream. For a hemisphere deep inside the roughness sublayer of a turbulent boundary layer, it is hard to extrapolate any scaling from these studies on isolated bodies in an external uniform flow.

In an attempt to capture the Re_t dependence of the shear stress patterns plotted in Figure 7, we plotted in Figure 11 the profiles of dimensionless mean shear stress along the hemisphere in the middle vertical plane of symmetry. The best collapse of these profiles on the same curve was obtained by testing different values of n for a Re_t^n dependence, and an optimum was found for $n = 0.26$ (Figure 12). Of course, the dimensionless shear stress on the hemispheres, even scaled by $\mu(u^*/h)Re_t^{0.26}$, still exhibits a slight dependence with the Reynolds number Re_t because the flow topology around the hemisphere is Re_t dependent. However, this scaling captures the overall shear stress intensity dependence, which is sufficient to explain the biomass accrual delay with increasing flow velocity in the three experiments of Moulin *et al*. (2008) and Graba *et al*. (2013).

The fact that colonization occurs preferentially around zero shear region indicates that a critical shear stress value could be applied at fixed time to delimitate a colonization pattern for the three different flow conditions. Around the stagnation point, the shear stress distribution exhibits a linear behaviour, as seen in Figure 12 for $\theta \approx 0.9$. This reads $\tau = \alpha r \mu u^* Re_t^{0.26}/h$, following the Re_t dependence discussed earlier, with α as a geometrical constant and r as the distance from the stagnation point along the hemisphere surface. For a fixed critical value of τ for colonized regions, the patch area would scale as r^2, yielding a $\left(u^* Re_t^{0.26}\right)^{-2}$ dependence. For the three experimental conditions of Moulin *et al*. (2008) and Graba *et al*. (2013), this Reynolds dependence would yield a relative colonized surface ratio equal to 1, 0.06 and 0.015, respectively. The apparent discrepancy with measurements of biomass or estimated colonized surfaces given in Table III is due to the fact that large patches are already colonized in the LV flow region, for which the linear development around stagnation points does not hold anymore. Indeed, for IV and HV regions where the colonization is still confined to regions near the front stagnation point, the prediction of the ratio between the two colonized surfaces would be $0.06/0.015 = 4.0$, in reasonable agreement

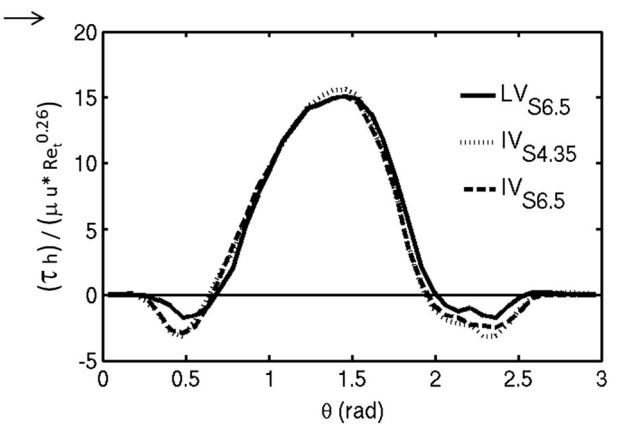

Figure 12. Same as Figure 11 with the best fit exponent (i.e. 0.26) for the *Re*-influence

with biomass measurements and estimated colonization surfaces from photographies (with ratios equal to 1.2–5.4 and 3.4, respectively; see Table III).

CONCLUSIONS

We have performed direct numerical simulations of a turbulent boundary layer flow over a bed of hemispheres (using an IBM method) in order to get a better understanding of the interaction between local hydrodynamics conditions and the ability for the epilithic biofilm to colonize and grow on a complex substrate. Detailed comparisons were made with river biofilm growth experiments performed in a hydraulic flume. Flow statistics above the substrates are shown to be in agreement with measurements performed by LDV and PIV in the experiments.

Access to local information in the canopy region allowed us to analyse the mean flow structure, turbulence statistics and wall parameters for various bed configuration, confinement and friction velocity. We found that the local wall shear stress (near the substrate) is the crucial parameter in the colonization and initial growth phases of biofilm. Biofilm will tend to first colonize regions of low-to-moderate wall shear stress and then spread over the whole substrate. The location of the regions of low shear stress obtained from the numerical simulations agrees reasonably well with that of the colonization regions observed in the experiments (see, e.g. Figure 7 versus Figures 8 and 10). This local shear stress τ on the surface of the hemispheres is shown to scale as $\mu(u^*/h)Re_t^{0.26}$, where $Re_t = u^* h/\nu$. The present scaling, together with a fixed critical shear stress for colonization and early growth, may explain the increasing delay in biomass accrual with increasing flow velocity in the experiments.

Ongoing effort is performed to extend this analysis so as to find a hydrodynamic criterion, which may allow to predict the possible surface of biofilm colonization on arbitrary substrate. This criterion may then be used in predictive models for biofilm biomass accrual.

ACKNOWLEDGEMENTS

F. C. was supported by a scholarship intended for PhD students partly founded by the Région Midi-Pyrénées. Some of the computational time was provided by the Scientific Groupment CALMIP (project P0930), the contribution of which is greatly appreciated.

REFERENCES

Asaeda T, Hong Son D. 2001. A model of the development of a periphyton community resource and flow dynamics. *Ecological Modelling* **137**: 61–75.

Battin T Sengschmitt D. 1999. Linking sediment biofilms, hydrodynamics, and river bed clogging: evidence from a large river. *Microbial Ecology* **37**: 185–196.

Biggs B, Hickey C. 1994. Periphyton responses to a hydraulic gradient in a regulated river in New Zealand. *Freshwater Biology* **32**(1): 49–59.

Biggs B, Thomsen H. 1995. Disturbance of stream periphyton by perturbations in shear stress: time to structural failure and differences in community resistance. *Journal of Phycology* **31**(2): 233–241.

Biggs B, Duncan M, Francoeur S Meyer W. 1997. Physical characterisation of microform bed cluster refugia in 12 headwater streams, New Zealand. *New Zealand Journal of Marine and Freshwater Research* **31**(4): 413–422.

Biggs B, Goring D, Nikora V. 1998. Subsidy and stress responses of stream periphyton to gradients in water velocity as a function of community growth form. *Journal of Phycology* **34**: 598–607.

Biggs B, Nikora V, Snelder T. 2005. Linking scales of flow variability to lotic ecosystem structure and function. *River Research and Applications* **21**(2-3): 283–298.

Biggs B, Ibbitt R Jowett I. 2008. Determination of flow regimes for protection of in-river values in New Zealand: an overview. *Ecohydrology and Hydrobiology* **8**(1): 17–429.

Bigot B, Bonometti T, Lacaze L, Thual O. 2012. A simple immersed-boundary method for solid-fluid interaction in constant and variable density flows. *in preparation*.

Boulêtreau S, Garabetian F, Sauvage S Sánchez-Pérez J. 2006. Assessing the importance of a self-generated detachment process in river biofilm models. *Freshwater Biology* **51**(5): 901–912.

Boulêtreau S, Izagirre O, Garabetian F, Sauvage S, Elosegi A, Sánchez-Pérez J. 2008. Identification of a minimal adequate model to describe the biomass dynamics of river epilithon. *River Research and Applications* **24**(1): 36–53.

Boulêtreau S, Sellali M, Elosegi A, Nicaise Y, Bercovitz Y, Moulin F, Eiff O, Sauvage S, Sánchez-Pérez J, Garabétian F. 2010. Temporal dynamics of river biofilm in constant flows: a case study in a riverside laboratory flume. *International Review of Hydrobiology* **95**(2): 156–170.

Boulêtreau S, Charcosset JY, Gamby J, Lyautey E, Mastrorillo S, Azémar F, Moulin F, Tribollet B, Garabetian F. 2011. Rotating disk electrodes to assess river biofilm thickness and elasticity. *Water Resource Research* **45**: 1347–1357.

Calmet I. 1995. Analyse par simulation des grandes échelles des mouvements turbulents et du transfert de masse sous une interface plane, PhD thesis.

Calmet I, Magnaudet J. 2003. Statistical structure of high-Reynolds-number turbulence close to the free surface of an open-channel flow. *Journal of Fluid Mechanics* (474): 355–378.

Castro I, Cheng H, Reynolds R. 2006. Turbulence over urban-type roughness: deductions from wind-tunnel measurements. *Boundary-Layer Meteorology* **118**(1): 109–131.

Cazelles B, Fontvieille D, Chau N. 1991. Self-purification in a lotic ecosystem: a model of dissolved organic carbon and benthic microorganisms dynamics. *Ecological Modelling* **58**: 91–117.

Cheng H, Castro I. 2002. Near wall flow over urban-like roughness. *Boundary-Layer Meteorology* **104**: 229–259.

Claret C, Fontvieille D. 1997. Characteristics of biofilm assemblages in two contrasted hydrodynamic and trophic contexts. *Microbial Ecology* **34**: 49–57.

Coceal O, Thomas T, Castro I Belcher S. 2006. Mean flow and turbulence statistics over groups of urban-like cubical obstacles. *Boundary-Layer Meteorology* **121**: 491–519.

Finnigan J. 2000. Turbulence in plant canopies. *Annual Review of Fluid Mechanics* **32**: 519–571.

Florens E. 2010. Couche limite turbulente dans les écoulements a surface libre: Etude expérimentale d'effets de macro-rugosités, PhD thesis, Université Paul Sabatier, Toulouse III.

Florens E, Eiff O, Moulin F. 2013. Defining the roughness sublayer and its turbulent statistics. *Experiments in Fluids* **54**: 1500, 15.

Fovet O, Belaud G, Litrico X, Charpentier S, Bertrand C, Dauta A, Hugodot C. 2010. Modelling periphyton in irrigation canals. *Ecological Modelling* **221**(8): 1153–1161.

Ghosh M, Gaur J. 1998. Current velocity and the establishment of stream algal periphyton communities. *Aquatic Botany* **60**(1): 1–10.

Graba M, Moulin F, Boulêtreau S, Garabétian F, Kettab A, Eiff O, Sánchez-Pérez J, Sauvage S. 2010. Effect of near-bed turbulence on chronic detachment of epilithic biofilm: experimental and modeling approaches. *Water Resources Research* **46**(11): 1944–7973.

Graba M, Sauvage S, Moulin F, Urrea G, Sabater S, Sanchez-Prez J. 2013. Interaction between local hydrodynamics and algal community in epilithic biofilm. *Water Research* **47**(7): 2153–2163.

Graba M, Sauvage S, Madji N, Mialet B, Moulin F, Urrea G, Buffan-Dubau E, Tackx M, Sabater S, Sanchez-Prez J. 2014. Interaction between local hydrodynamics and algal community in epilithic biofilm, *accepted in Freshwater Biology* .

Hondzo M, Wang H. 2002. Effects of turbulence on growth and metabolism of periphyton in a laboratory flume. *Water Resources Research* **38**(12): 1277–1285.

Horner RR, Welch EB, Veenstra RB. 1983. Periphyton of freshwater ecosystems, Vol. 17, Proceedings of the First International Workshop on Periphyton of Freshwater Ecosystems, held in Vaxjo, Sweden, 14–17 september 1982, Springer Netherlands, R. G. Wetzel, Dr. W. Junk, The Hague, Netherlands.

Kim J, Moin P, Moser R. 1987. Turbulence statistics in fully-developed channel flow at low Reynolds-number. *Journal of Fluid Mechanics* **28**: 133–166.

Kim B, Jackman A, Triska F. 1992. Modeling biotic uptake by periphyton and transient hyporheic storage of nitrate in a natural stream. *Water Resources Research* **28**(10): 2743–2752.

Labiod C, Godillot R, Caussade B. 2007. The relationship between stream periphyton dynamics and near-bed turbulence in rough open-channel flow. *Ecological Modelling* **209**(2-4): 78–96.

Luce J, Cattaneo A, Lapointe M. 2010. Spatial patterns in periphyton biomass after low-magnitude flow spates: geomorphic factors affecting patchiness across gravel–cobble riffles. *Journal of the North American Benthological Society* **29**(2): 614–626.

Macdonald R. 2000. Modelling the mean velocity profile in the urban canopy layer. *Boundary-Layer Meteorology***97**: 25–45.

Matthaei C, Guggelberger C, Huber H. 2003. Local disturbance history affects patchiness of benthic river algae. *Freshwater Biology* **48**: 1514–1526.

Mignot, E., Barthelemy, E. Hurther, D. , 2009. Double-averaging analysis and local flow characterization of near-bed turbulence in gravel-bed channel flows. *Journal of Fluid Mechanics* (618): 279–303.

Moulin F, Peltier Y, Bercovitz Y, Eiff O, Beer A, Pen C, Bouletreau S, Garabetian F, Sellali M, Sanchez-Perez J, Sauvage S, Baque D. 2008. Experimental study of the interaction between a turbulent flow and a river biofilm growing on macrorugosities. In '8th International Conference on Hydro-science and Engineering, ICHE2008, 8–12 September 2008, Nagoya, Japan'.

Nezu I, Nakagawa H. 1993. Turbulence in Open-Channel Flows. IAHR Monograph Series. A.A. and Balkema: Rotterdam, The Netherlands.

Nikora V, Goring D, Biggs B. 2002. Some observations of the effects of micro-organisms growing on the bed of an open channel on the turbulence properties. *Journal of Fluid Mechanics* **450**: 317–341.

Nikora V, McEwan I, McLean S, Coleman S, Pokrajac D, Walters R. 2007a. Double-averaging concept for rough-bed open-channel and overland flows: theoretical background. *Journal of Hydraulic Engineering* **133**(8): 873–883.

Nikora V, McLean S, Coleman S, Pokrajac D, McEwan I, Campbell L, Aberle J, Clunie D, Koll K. 2007b. Double-averaging concept for rough-bed open-channel and overland flows: applications. *Journal of Hydraulic Engineering* **133**(8): 884–895.

Pokrajac D, Campbell L, Nikora V, Manes C, McEwan I. 2007. Quadrant analysis of persistent spatial velocity perturbations over square-bar roughness. *Experiments In Fluids* **42**(3): 413–423.

Power M, Stewart A. 1987. Disturbance and recovery of an algal assemblage following flooding in an Oklahoma stream. *American Midland Naturalist* **117**(2): 333–345.

Raupach M, Antonia R, Rajagopalan S. 1991. Rough-wall turbulent boundary layers. *Applied Mechanics Reviews* **44**(1): 1–25.

Reiter M. 1986. Interactions between the hydrodynamics of flowing water and the development of a benthic algal community. *Journal of Freshwater Ecology* **3**(4): 511–517.

Riber H, Wetzel R. 1987. Boundary-layer and internal diffusion effects on phosphorus fluxes in lake periphyton. *Limnology and Oceanography* **32**: 1181–1194.

Robinson C, Uehlinger U, Monaghan M. 2004. Stream ecosystem response to multiple experimental floods from a reservoir. *River Research and Applications* **20**: 359–377.

Saravia L, Momo F, Boffi Lissin L. 1998. Modeling periphyton dynamics in running water. *Ecological Modelling* **114**(1): 35–47.

Stevenson R, Bothwell M, Lowe R. 1996. An Introduction to Algal Ecology in Freshwater Benthic Ecosystems Habitats. Academic Press: San Diego.

Takao A, Kawaguchi Y, Minagawa T, Kayaba Y, Morimoto Y. 2008. The relationships between benthic macroinvertebrates and biotic and abiotic environmental characteristics downstream of the Yahagi dam, central Japan, and the state change caused by inflow from a tributary. *River Research and Applications* **24**: 580–597.

Uehlinger U, Bührer H, Reichert P. 1996. Periphyton dynamics in a floodprone prealpine river: evaluation of significant processes by modelling. *Freshwater Biology* **36**(2): 249–263.

Yuki Y, Takeuchi S, Kajishima T. 2007. Efficient immersed boundary method for strong interaction problem of arbitrary shape object with the self-induced flow. *Journal of Fluid Science and Technology* **2**(1): 1–11.